

# Extending a Linear Kernel-driven BRDF Model to Realistically Simulate Reflectance Anisotropy over Rugged Terrain

Kai Yan, Hanliang Li, Wanjuan Song, Yiyi Tong, Dalei Hao, Yelu Zeng, Xihan Mu,

Guangjian Yan, Senior Member, IEEE, Yuan Fang, Ranga B. Myneni and Crystal Schaaf

**Abstract**—Bidirectional Reflectance Distribution Function (BRDF) models are used to correct surface bidirectional effects and estimate land surface albedo. Many operational BRDF/Albedo algorithms adopt a Roujean Linear Kernel-driven BRDF (RLKB) model because of its simple form and good performance in fitting multi-directional surface reflectance values. However, this model does not explicitly consider topographic effects, resulting in errors when applied over rugged terrain. To address this issue, we proposed a hybrid algorithm suitable for both flat and rugged terrain, called Topographical Kernel-Driven (Topo-KD). First, we constructed a Linear Kernel-driven BRDF model considering Terrain (LKB\_T) which describes the topographic effects with a Mountain Radiative Transfer (MRT) model. Then, the Topo-KD algorithm adaptively selects the most suitable model (RLKB or LKB\_T) according to terrain conditions and fitting residuals. The performances of Topo-KD and RLKB using the RossThick-LiSparseReciprocal (RTLSR) kernel are compared using simulated datasets and MODIS observations. The results show that the BRDF of the pixel is affected by topography. But the RTLSR model does not specifically account for it, resulting in larger biases over rugged terrain than the Topo-KD algorithm in both the red and Near Infrared (NIR) bands. And the experiment using MODIS datasets demonstrates that the Topo-KD algorithm reduces fitting residuals in the red and NIR bands by 21.5% and 27.4% compared with the RTLSR model. These results indicate that the Topo-KD algorithm can be a better choice for retrieving land surface parameters and describing the radiative transfer process in mountainous areas.

**Index Terms**—BRDF/Albedo, DEM, Kernel-driven model, Radiative transfer, Reflectance anisotropy, Topographic effects

This work was supported by the National Natural Science Foundation of China (41901298 and 42090013), the Open Fund of State Key Laboratory of Remote Sensing Science (OFSLRSS201924), and the Fundamental Research Funds for the Central Universities (2652018031).

K. Yan and H. Li are with the School of Land Science and Techniques, China University of Geosciences, Beijing 100083, China. (e-mail: kaiyan@cugb.edu.cn; lihanliang1998@cugb.edu.cn).

W. Song is with the Aerospace Information Research Institute, China Academy of Sciences, Beijing 100083, China (e-mail: songwj@aircas.ac.cn).

Y. Tong, X. Mu and G. Yan are with the State Key Laboratory of Remote Sensing Science, Beijing Normal University, Beijing, 100101, China (e-mail: tongyiyi0311@163.com; muxihan@bnu.edu.cn; gjyan@bnu.edu.cn).

## I. INTRODUCTION

BIDIRECTIONAL Reflectance Distribution Functions (BRDFs) are widely used to describe the reflective properties of a non-Lambertian surface. Several land-surface BRDF models have been developed for four main applications: 1) to generate measures of surface albedo; 2) to correct bidirectional effects, which can add significant noise-like fluctuations to time series [1-3]; 3) to serve as lower boundary conditions for atmospheric Radiative Transfer (RT) models [4, 5]; and 4) to estimate Leaf Area Index (LAI) and other important parameters for global ecological and environmental monitoring [6-8].

Rugged terrain affects the pixel's BRDF, but current models/algorithms, which have been designed for uniform terrain conditions, do not explicitly account for topographic effects when estimating land surface albedo and retrieving biophysical-structural properties [9-11]. However, many studies have shown that remote sensing signals are affected by rugged terrain [12, 13]. Topography affects the spatial distribution of downward radiation in coarse pixels and changes the local sun-canopy-sensor geometry of each subpixel [14, 15]. Topographic effects in coarse-resolution data are often overlooked because they are difficult to estimate and the overall slope is usually small. However, the BRDF of a coarse remote sensing pixel over rugged terrain shows differences from that over flat terrain [16, 17]. Therefore, to more accurately model the BRDF over rugged terrain, it is necessary to develop a model that can capture the topographic effects.

Since the early 1980s, many physical and empirical methods

D. Hao is with the Atmospheric Sciences and Global Change Division, Pacific Northwest National Laboratory, Richland, WA 99352, USA. (e-mail: dalei.hao.93@gmail.com).

Y. Zeng is with the Joint Global Change Research Institute, Pacific Northwest National Laboratory, College Park, MD 20740, USA. (e-mail: zengyelu@163.com).

Y. Fang is with the Department of Systems Design Engineering, University of Waterloo, Canada. (e-mail: y227fang@uwaterloo.ca).

R.B. Myneni is with the Department of Earth and Environment, Boston University, Boston, MA 02215, USA. (e-mail: rmyneni@bu.edu).

C. Schaaf is with the School for the Environment, University of Massachusetts, Boston, MA 02125, USA. (e-mail: crystal.schaaf@umb.edu).

Correspondence should be addressed to X. Mu (muxihan@bnu.edu.cn) and G. Yan (gjyan@bnu.edu.cn).

have been proposed for dealing with topographic effects. The Geometric Optical Mutual Shadowing with Topography (GOMST) model has been used to model the BRDF of a slope by using the sun-terrain-sensor geometric correction from the horizontal plane to the local terrain. [18, 19]. Yin et al. [20] developed the Path Length Correction (PLC)-based model for simulating canopy reflectance over rugged terrain. Although they have been proven reliable for simulating the bidirectional reflectance over rugged terrain, these methods regard the pixel as a “single slope” without subpixel effects. This may be acceptable for high-resolution data, such as Landsat Thematic Mapper (TM) imagery (30 m). But for coarse pixels, such as a Moderate-resolution Imaging Spectroradiometer (MODIS) pixel (500 m), their directional reflectance can be affected not only by the overall slope and aspect of the rugged terrain, but also by the spatial distribution of these subpixel slopes [21]. Thus, these methods, which do not consider the influence of subpixels, may not perform well at larger resolutions.

To address this issue, and more accurately describe the RT process among slopes, Mountain Radiative Transfer (MRT) models have been developed to simulate the coarse pixel’s BRDF by considering terrain blocking-effects using a DEM and sun-sensor geometry information [22, 23]. Based on the MRT theory, Wen et al. [10] developed a physically-based Equivalent Slope Model (ESM) to characterize the clear-sky reflectance anisotropy of a coarse pixel over rugged terrain, based on the assumption that there is an equivalent virtual smooth slope whose incoming and outgoing radiation will be the same as that of the coarse pixel. Hao et al. [24] put forward a diffuse-ESM (dESM) that takes into account terrain altered diffuse skylight, and Hao et al. [25] further developed an improved Topography-Coupled Kernel-Driven (TCKD) reflectance model with a correction of diffuse skylight effects, based on the dESM. However, both the dESM and TCKD model neglect the remainder of the Taylor expansion in the construction, which can cause approximation errors. These models also neglect any additional multiple-scattering effects caused by adjacent terrain-reflected radiance that may account for a large portion of the downward radiance in extremely rugged terrain [15].

The Roujean Linear Kernel-driven BRDF (RLKB) model, as a semi-empirical model, can easily utilize the reflectance of directional satellite observations and use a simple semi-empirical linear formula to estimate the surface BRDF. Such a semiempirical linear kernel-driven BRDF model, using the RossThick-LiSparseReciprocal (RTLSR) kernel has been adopted by the operational MODIS BRDF/Albedo algorithm [18, 26-28], which relies on the weighted sum of an isotropic parameter and two kernels of sun-sensor geometry to determine the bidirectional reflectance [29-31]. The linear nature of these models has the significant advantage that the coefficient of each kernel can easily be used either to calculate the reflectance as a function of sun-sensor geometry or to estimate albedos in conjunction with a Look-Up Table (LUT) of pre-computed kernel integrals. Although these BRDF models have been proven to fit most land surfaces, they do not explicitly consider topography and may lead to errors in mountainous areas [9].

Therefore, there is interest in developing a BRDF algorithm

that can be applied to both flat and rugged terrain used as a new operational algorithm. In this study, we proposed a Linear Kernel-driven BRDF model considering Terrain (LKB\_T) by coupling the MRT model with the RLKB model using the RTLSR kernel. Compared with the recent TCKD model [25], the LKB\_T model has an advantage in that it considers terrain induced multiple-scattering effects and has a rigorous mathematical foundation without a Taylor expansion approximation. Additionally, LKB\_T has the ability to model mixed pixels with high-resolution observations as auxiliary data. To obtain a wider range of applications, in this study, we combined the RLKB and the LKB\_T models into a hybrid algorithm, Topographical Kernel-Driven (Topo-KD), which not only serves to more appropriately model the retrieved accuracy over rugged terrain but also retains the advantages of the RLKB model. The Topo-KD algorithm was evaluated and validated using simulated data and MODIS observations compared with the RLKB model by using RTLSR kernels, and its advantages, the limitations of this study were discussed.

## II. DATASETS AND METHODOLOGY

### A. Datasets and Study Area

TABLE I  
QUALITY SCREENING FOR MOD/MYD09GA DATASETS

1km QA	Cloud	Clear
	Cloud shadow	No
	Land water	Land
	Aerosol	Not high
	Cirrus	None or small
	Internal cloud	No
	Adjacent cloud	No
	Snow or Ice	No
500m QC	Band quality	Highest quality

MODIS is a key instrument onboard the Terra and Aqua satellites. Terra MODIS and Aqua MODIS observe the entire Earth’s surface every 1 to 2 days, acquiring data in 36 spectral bands. Based on an optical mechanical scanning technology, the Field of View (FOV) of MODIS can change from  $-55^\circ$  to  $+55^\circ$ , allowing MODIS to provide multi-angular reflectance from several days of observations. The MOD/MYD09GA products, derived from MODIS observations, provide daily surface BRF at a gridded 500 m spatial resolution and for seven spectral bands [32]. Only the red band and the Near Infrared (NIR) band (centered at 648 nm and 858 nm respectively) were used in this study. By considering the 1 km reflectance data state Quality Assurance (QA) and the 500 m Quality Control (QC), we extracted the gridded 500 m multi-angular observations for thirty days, from 1 Dec. 2009 to 30 Dec. 2009, and synthesized a multi-angle observation dataset. Table. 1 lists the thresholds we used to control the quality of this dataset.

We selected a 46 km  $\times$  46 km mountainous area in the Tibetan Plateau ( $98^\circ32' - 98^\circ31'29''\text{E}$ ,  $29^\circ32'7'' - 29^\circ57'1''\text{N}$ ) as the study area, and a DEM with 1 arc-second spatial resolution from the Advanced Spaceborne Thermal Emission and Reflection Radiometer global DEM version 2 (ASTER GDEM2, <https://lpdaac.usgs.gov/>) dataset was projected to equal-area and used to describe the topography (Fig. 1).

Considering that the footprint of the imaging sensor expands with the VZA, that high heterogeneity in mountainous areas all can introduce high uncertainty into the multi-angular dataset [33]. And due to the high FOV of MODIS, the projection of a MODIS detector's Instantaneous FOV (IFOV) onto the surface is approximately 2.0 and 4.8 times larger than at nadir along track and scan directions at the scan edge [32]. This will introduce panoramic error and further to lead a data repetition [34]. To avoid these effects, we upscaled 16 MODIS pixels (460 m) to a coarse (1840 m) pixel. The whole study area contains 625 coarse pixels, and each coarse pixel contains 2116 DEM pixels.

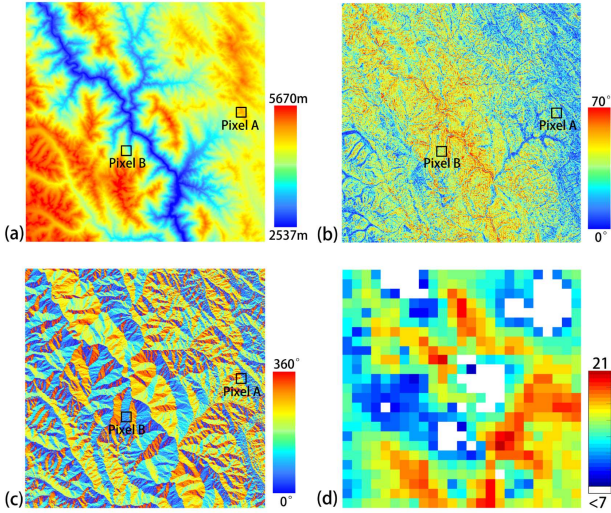


Fig. 1. Topographical conditions of the test mountainous area. (a) DEM of the whole region; (b) and (c) are slope and aspect distribution, respectively; (d) Number of available observations in MOD09GA data. The Pixel A and B marked in panel (a), (b), and (c) are the example coarse pixels in Fig. 5.

During these days, the mean local SZA was  $55^\circ$  at the imaging time, causing the presence of terrain induced shadows in the data. Fig. 1 (d) shows the number of valid observations for each coarse pixel (pixels with less than seven observations are left blank) in MOD09GA data. The maximum number of observations can reach 21, and 90% of the pixels (560 in total) with at least seven observations were used to test the Topo-KD algorithm.

## B. BRDF Modeling for All Terrains

### 1) Kernel-driven Model for Flat Terrain

The initial equation of the RLKB model [2] is given by Roujean et al. as:

$$R(\theta_i, \theta_v, \varphi, \Lambda) = f_{iso}(\Lambda) + f_{vol}(\Lambda)K_{vol}(\theta_i, \theta_v, \varphi) + f_{geo}(\Lambda)K_{geo}(\theta_i, \theta_v, \varphi) \quad (1)$$

where  $K_{vol}$  and  $K_{geo}$  represent the volume-scattering and the geometric-optical scattering kernels, respectively, which are functions consisting of the Solar Zenith Angle (SZA,  $\theta_i$ ), the View Zenith Angle (VZA,  $\theta_v$ ) and the Relative Azimuth Angle

(RAA,  $\varphi$ ). The weight coefficients ( $f_{iso}$ ,  $f_{vol}$  and  $f_{geo}$ ) represent the weight of isotropic scattering, volume-scattering, and geometric-optical scattering kernels.  $R(\theta_i, \theta_v, \varphi, \Lambda)$  represents the Bidirectional Reflectance Factor (BRF) of the corresponding band  $\Lambda$ . According to the least-squares method, the optimal weight coefficients can be retrieved theoretically from at least a minimum number of three observations, although since practically an adequate sampling of the viewing hemisphere is needed; at least 7 well distributed observations are required. Once an appropriate high quality BRDF model has been retrieved, reflectance in other sun-sensor geometries can then be calculated using these coefficients and the corresponding kernels.

The RossThick and LiSparseR kernels have been selected for the current operational MODIS BRDF/albedo algorithm. The RossThick kernel is a single-scattering approximation of the RT theory by Ross [26] consisting of a layer of small scatterers with uniform Leaf Angle Distribution (LAD), a Lambertian background, and equal leaf transmittance and reflectance. The LiSparseR kernel is a reciprocal form of the LiSparse kernel, which is derived from the geometric-optical mutual shadowing BRDF model by Li and Strahler [7, 18]. Several studies have identified this RossThick-LiSparseR kernel combination as the best model for the operational MODIS BRDF/Albedo algorithm [27, 35, 36]. However, the RLKB models assume that the land-surface BRDF shape is symmetrical with regard to the azimuth. Because of topographic effects, this assumption is unacceptable over rugged terrain.

### 2) Kernel-driven Model for Rugged Terrain

An MRT model has been shown to represent primary topographic effects well with a high-resolution ( $< 50$  m) DEM, (currently available for most land surfaces) [37]. Here we have adapted an RLKB model to rugged terrain by coupling the RLKB model using RTLSR kernel and the MRT model and constructing a new model, LKB\_T.

Research has suggested that the amount of topographic effects depends on the spatial resolution of the DEM [38]. Here, we assume that a DEM with a resolution higher than 50 m can fully capture the topographic variation of a surface with no micro-area topographic effects within the pixel [39]. As with earlier studies (e.g., Gao et al. 2012; Wen et al. 2008), each coarse pixel is first divided into small, smooth hill slopes (subpixels) that have different but known slopes, aspects and areas (Fig. 2) and the sun-sensor geometry is then rotated with respect to these gradients and aspect angles. The equivalent geometry was therefore introduced for this coordinate transformation, and the two local kernel functions for each subpixel were calculated. Note that the two kernel forms refer to direct and diffused radiation and have different reflectance features: BRDF kernels and Hemispheric-Directional Reflectance (HDR) kernels. For direct solar radiation, we have used two traditional BRDF kernels ( $k_{vol}(\theta_i, \theta_v, \varphi)$  and  $k_{geo}(\theta_i, \theta_v, \varphi)$ ), which are functions of both sun and sensor geometries, to describe the reflectance characteristic. For sky

diffuse and adjacent-terrain reflected radiation, a hemispheric-directional reflectance is more suitable and so we incorporated two so-called ‘‘HDR kernels’’ ( $h'_{vol}(\theta_v)$  and  $h'_{geo}(\theta_v)$ ), which are functions of only the position of the sensor [40]. Since the two adopted BRDF kernels are reciprocal, ‘‘HDR kernels’’ are equal in value to ‘‘Directional-Hemispheric Reflectance (DHR) kernels’’ ( $h_{vol}(\theta_s)$  and  $h_{geo}(\theta_s)$ ), which can be obtained from the existing LUT [7].

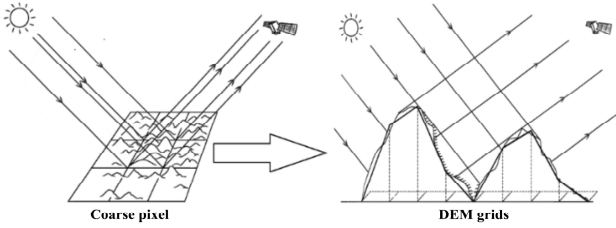


Fig. 2. The topography of each coarse pixel can be described as several sunlit and shaded slopes using a high-resolution DEM.

For a mountainous surface, the coarse pixels’ kernel functions are obtained using a weighted mean. The MRT model, which describes the distribution of incoming energy and its transfer process among the subpixels, is used to calculate these weights (See Appendix B) and serves as the bridge for upscaling from subpixels to a coarse pixel. Consequently, the coarse pixels’ redefined kernel functions ( $Ker^l_{iso}$ ,  $Ker^l_{vol}$ , and  $Ker^l_{geo}$ ), which we call integrated kernels, can be expressed as:

$$Ker^l = \frac{\sum_{i=1}^m \sum_{j=1}^n [\Theta_{v_{i,j}} \mu_{v_{i,j}} Ker^{local}_{i,j} E_{i,j}^{incoming}]}{(\cos(\theta_s) + k) \sum_{i=1}^m \sum_{j=1}^n [\Theta_{v_{i,j}} \mu_{v_{i,j}} / \cos(S_{i,j})]} \quad (2)$$

where  $m$  and  $n$  are the lines and samples of the subpixels,  $\theta_s, \theta_v, S, k$  are the SZA, VZA, slope, and fraction of diffuse sky, respectively.  $\Theta_{v_{i,j}}$  and  $\mu_{v_{i,j}}$  are the terrain blocking indicator and the projection coefficient of view direction for the subpixel  $(i, j)$ .  $Ker^{local}$  is the local kernel function of a single slope. Its matrix form can be written as:

$$Ker^{local}_{i,j} = \begin{pmatrix} 1 & 1 \\ k_{vol_{i,j}} & h_{vol_{i,j}} \\ k_{geo_{i,j}} & h_{geo_{i,j}} \end{pmatrix} \quad (3)$$

where  $k_{vol_{i,j}}$  and  $k_{geo_{i,j}}$  are subpixel BRDF kernels for volume-scattering and geometric-optical scattering; similarly,  $h_{vol_{i,j}}$  and  $h_{geo_{i,j}}$  are DHR kernels.

$E_{i,j}^{incoming}$  is the normalized received energy of the subpixel  $(i, j)$  and includes three parts (solar direct radiance, sky diffuse radiance and adjacent terrain-reflected radiance), its matrix form can be written as:

$$E_{i,j}^{incoming} = \begin{pmatrix} \Theta_{s_{i,j}} \mu_{s_{i,j}} / \cos(S_{i,j}) \\ (kV_{d_{i,j}} + K_{i,j}) / \cos(S_{i,j}) \end{pmatrix} \quad (4)$$

where  $\Theta_{s_{i,j}}$  and  $\mu_{s_{i,j}}$  are the shelter indicator and the projection coefficient of the sun’s direction for subpixel  $(i, j)$ .  $V_{d_{i,j}}$  and  $K_{i,j}$  are the sky view factor and terrain-reflected irradiance factor, respectively [41].

By using the MRT model to describe the RT process between subpixel slopes (terrain blocking, multi-reflecting), these three integrated kernels now contain the topographic effects. As with an RLKB model, the three weight coefficients ( $F_{iso}$ ,  $F_{vol}$  and  $F_{geo}$ ), which represent the weights of isotropic scattering, volume-scattering and geometric-optical scattering, are introduced to calculate the BRF using the following formula:

$$R(\theta_i, \theta_v, \varphi, \Lambda, DEM) = F_{iso}(\Lambda) Ker^l_{iso}(\theta_i, \theta_v, \varphi, DEM) + F_{vol}(\Lambda) Ker^l_{vol}(\theta_i, \theta_v, \varphi, DEM) + F_{geo}(\Lambda) Ker^l_{geo}(\theta_i, \theta_v, \varphi, DEM) \quad (5)$$

where  $R(\theta_i, \theta_v, \varphi, \Lambda, DEM)$  represents the BRF of the corresponding band  $\Lambda$ .

Note that the LKB\_T model (Eq. (5)) has the same form as the RLKB model (Eq. (1)). When the terrain is uniformly flat, then the LKB\_T is the same as the RLKB, and thus the RLKB model is a specific case of the LKB\_T model. The reflectance for any other sun-sensor geometries can then be calculated using these coefficients.

### 3) Self-adaptation to Terrain Mode

In order to guarantee the reliability of the fitting results and retain the advantages of the RLKB model, we propose a hybrid algorithm that combines efficiency and accuracy by using both LKB\_T and RLKB models and name the algorithm Topo-KD. And we define a Terrain Asymmetry Index (TAI) to classify the terrain properties of the pixels to improve computing efficiency. The TAI is calculated as:

$$TAI = \sqrt{\sum_{i=1}^n (Num_i - PixelNum / n)^2} \quad (6)$$

where the  $360^\circ$  azimuth is divided into  $n$  major directions, and  $Num_i$  refers to the number of the aspects of subpixels in the  $i$ -th major direction,  $PixelNum$  is the total number of subpixels in a coarse pixel. The TAI essentially describes the aspect distribution in a coarse pixel. In this paper, we divided the  $360^\circ$  azimuth into 18 directions with a step of  $20^\circ$  ( $n$  is 18, the central azimuths of the 18 directions are  $0^\circ, 20^\circ, 40^\circ, 60^\circ, \dots$ ).

Fig. 3 shows the workflow of the Topo-KD algorithm. First, the mean slope, aspect, and TAI of each coarse pixel are calculated. Then, the coarse pixels are divided into flat pixels and rugged pixels according to the Slope Threshold (ST) and TAI Threshold (TT). If the pixel’s mean slope is larger than the ST, and its TAI is larger than the TT, it is classified as a rugged pixel, otherwise it is classified as a flat pixel. Finally, for rugged



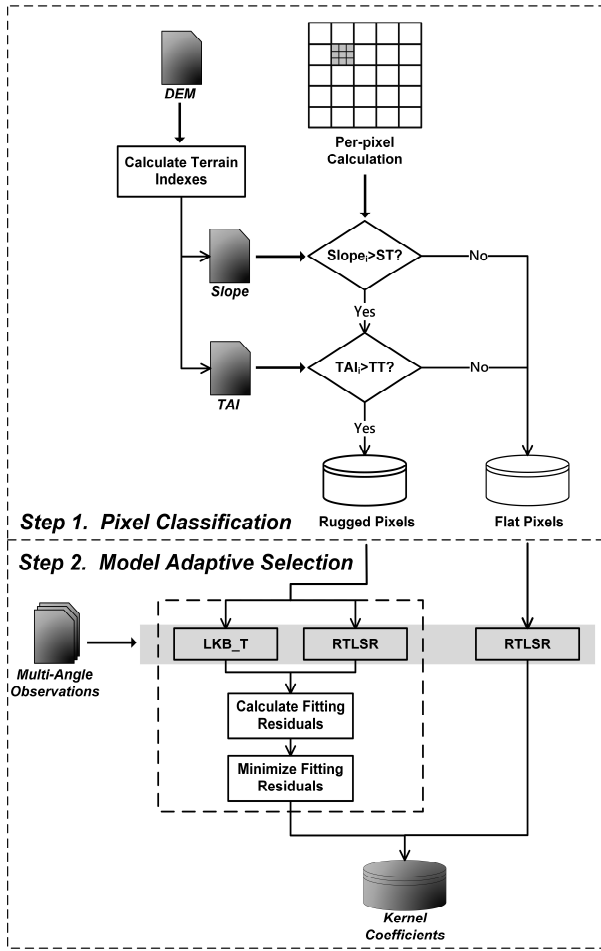


Fig. 3. Calculation process of the Topo-KD algorithm. Slope<sub>i</sub> and TAI<sub>i</sub> are slope and terrain asymmetry index of each coarse pixel. ST and TT are the slope threshold and TAI threshold, respectively.

pixels, both kernel models (RLKB and LKB\_T) are triggered for a comparison of the fitting residuals. The model results with smaller fitting residuals are selected as output. For flat pixels, only the RLKB model is used (with whatever kernel combination is being utilized, RTLRSR is used in this paper) for higher computation efficiency. Note that the ST and TT are adjustable parameters for a trade-off between accuracy and efficiency. In order to fully compare the fitting ability of the Topo-KD algorithm and the RLKB model, in this paper, both the ST and TT are set to 0.

### C. Simulation-based Evaluation

Although many field campaigns have been conducted and a growing number of ground-based observation sites are available for the validation of the BRDF models, a quantitative evaluation of these models in mountainous areas remains a daunting challenge [42, 43]. Therefore, we want to know if a model that takes into account topography capture the reflectance of a rugged terrain. Here, we answer these questions by using simulated data based on the MRT model to compare the performance of the RLKB model with that of the Topo-KD algorithm using RTLRSR kernel in the study area.

Based on the MRT model, the bidirectional reflectance of a

coarse pixel can be expressed by the reflectance of each subpixel's slope. If the BRF and HDR of each slope are known, we can obtain the pixel's BRF for any direction. We use the hotspot version of the light Scattering by the Arbitrarily Inclined Leaves model (SAILH) [44] to calculate the subpixels' BRF and HDR, and then simulate the coarse pixels' bidirectional reflectance. This canopy reflectance model assumes that the canopy is a homogeneous semi-infinite medium with Lambertian leaves, characterized by their reflectance and transmittance spectra ( $r_l$  and  $t_l$ ). Soil reflectance ( $r_s$ ) is specified at the lower boundary. Canopy structure is characterized by the LAI and the average LAD value. The hotspot effect is modeled using the ratio between leaf size and canopy height (HSF). Additional variables characterize the sun-sensor geometry ( $\theta_s$ ,  $\theta_v$ ,  $\varphi_s$ ,  $\varphi_v$ ) and the fraction of diffuse illumination ( $k$ ). Note that we used the ellipsoidal leaf inclination distribution with random azimuth orientation ( $\theta_m$  and  $\varepsilon$ ). The input parameters for the SAILH model are listed in Table. 2.

TABLE II  
INPUT SETTING FOR SAILH SIMULATIONS

Parameters	Description	Red band	NIR band
$\theta_m$	Average leaf angle	45°	45°
$\varepsilon$	Elliptical eccentricity	0.10	0.10
HSF	Hot spot factor	0.10	0.10
$k$	Fraction of diffused sky irradiance	0.10	0.10
$r_l$	Leaf reflectance	0.0546	0.4957
$t_l$	Leaf transmittance	0.0149	0.4409
$r_s$	Soil reflectance	0.1270	0.1590
LAI	Leaf area index	4	4

For each coarse pixel, there were two simulated datasets under the sun direction  $\theta_s=55^\circ$  and  $\varphi_s=160^\circ$  and  $\theta_s=55^\circ$  and  $\varphi_s=210^\circ$  (The sun directions are from MOD09DA and MYD09GA data) in both the red and NIR bands were simulated using our forward BRDF simulation method. We simulated 576 (16 VZAs  $\times$  36 VAAs) sun-sensor geometries under each sun direction, the VZA ranged from  $0^\circ$  to  $75^\circ$  with a step of  $5^\circ$ ; the View Azimuth Angle (VAA) ranged from  $0^\circ$  to  $350^\circ$  with a step of  $10^\circ$ . We extracted simulated BRF in 32 sun-sensor geometries (shown in Fig. 4) from two simulated datasets as input data for the RTLRSR model and the Topo-KD algorithm. To fit the reality, the 32 sun-sensor geometries are from MODIS observation data and we sampled the BRF in these directions with corresponding method for two simulated datasets (The simulated dataset under  $\theta_s=55^\circ$  and  $\varphi_s=160^\circ$  was sampled with the black dots in Fig. 4, the other simulated dataset was sampled with the blue dots). Then we used the coefficients retrieved by the input data to predict the BRF for other view directions under the sun direction  $\theta_s=55^\circ$  and  $\varphi_s=160^\circ$ . The comparisons between simulated and predicted BRF were used

to quantitatively evaluate the performance of RTLSR and Topo-KD through the determination coefficient ( $R^2$ ), the Root-Mean-Square-Error (RMSE), the normalized RMSE (nRMSE) and the bias:

$$\left\{ \begin{array}{l} R^2 = \frac{\left[ \sum_{i=1}^n (y_i - \bar{y})(x_i - \bar{x}) \right]^2}{\sum_{i=1}^n (y_i - \bar{y})^2 \times \sum_{i=1}^n (x_i - \bar{x})^2} \\ RMSE = \sqrt{\frac{1}{n-1} \sum_{i=1}^n (y_i - x_i)^2} \\ nRMSE = \frac{RMSE}{\bar{x}} \\ bias = \text{mean}(y - x) \end{array} \right. \quad (7)$$

where  $n$  is the total number of angles,  $x$  and  $y$  are simulated and predicted BRDF, respectively.

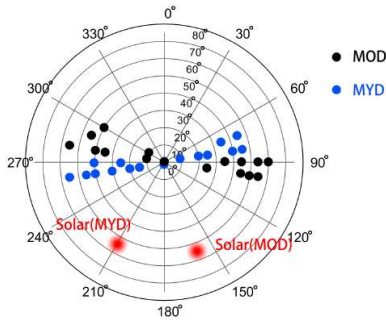


Fig. 4. Distribution of sampled angles for model evaluation. The angles represented by black and blue dots are from MOD09GA and MYD09GA data.

#### D. Observation-based Validation

The multi-angular satellite observations dataset mentioned above can provide reflectance data and sun-sensor geometries information. Both RTLSR and Topo-KD can use the dataset to fit the kernel coefficients and then estimate the entire hemispherical BRDF. We used the coefficients retrieved from Terra-MODIS observations to predict those observations from Aqua-MODIS and evaluated the accuracy of the predictions. We then calculated the RMSE and  $R^2$  between the predicted and the observed values of Aqua MODIS and compared the performance of the RTLSR model and the Topo-KD algorithm.

### III. RESULTS

#### A. Evaluation of the LKB\_T Model Based on Simulated Data

Here, we used simulated data to compare the new proposed LKB\_T model with the RTLSR model on the pixels, and the effect of rugged terrain on the BRDF shape of the pixel can be observed. Taking two pixels with small (Pixel A, Fig. 5 (a)) and large (Pixel B, Fig. 5 (b)) TAI and different slope as examples, we compared the influence of terrain on the BRDF characteristics. We can see that the aspects of pixel A is relatively uniformly distributed in all major directions and has a smaller slope compared to Pixel B, lead its simulated BRDF shape in the red and NIR bands is almost symmetric around the Solar Principal Plane (SPP). On the contrary, the pixel B present irregularly BRDF distributions, especially in the large VZA direction (Fig. 5 (b-2) and (b-3)), which is caused by

topographic effects. The simulated BRDF shapes in the red and NIR bands of these two pixels are similar, suggesting that topography has similar effects on different spectral bands. The above results indicate that topographic variations in a pixel lead to the irregular wrinkles in the BRDF shapes.

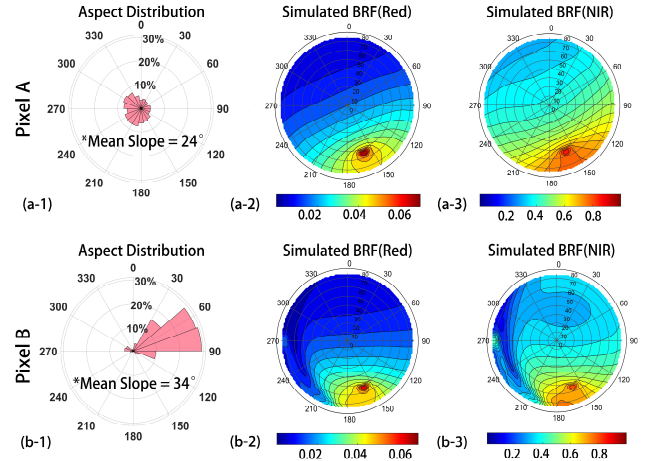


Fig. 5. Aspect distribution and simulated BRDF shapes of two pixels with small (Pixel A) and large (Pixel B) TAI. (a-1) and (b-1) are the distributions of the aspect of the two pixels, the percentages on the concentric circles mean the proportion of DEM pixels in each direction. The contour plots show the BRDF shapes of two pixels, (a-2) and (b-2) are BRDF values in the red band, (a-3) and (b-3) are BRDF values in the NIR band. The positions of the two pixels are marked in Fig. 1.

In Fig. 6, we compared the performance of the RTLSR and LKB\_T models on the pixels with rugged terrain (Pixel B in Fig. 5). The BRDF anisotropies for Pixel B in both the red and NIR bands are pronounced, especially in the large VZA region. There is a big difference between the RTLSR predicted BRDF shapes and simulated BRDF shapes for the red and NIR bands: In Fig.6 (a-2) and (b-2), they are strictly symmetric about the SPP (shown with red lines), which is determined by the symmetrical kernels of the RTLSR model, but the simulated BRDF shapes do not show symmetry about the SPP. On the contrary, the predicted BRDF shapes of the LKB\_T model (shown in Fig.6 (a-3) and (b-3)) are very similar to the simulated BRDF shapes. it's worth noting that there is a change in BRDF values caused by the terrain in Fig.6 (a-1) and (a-2) when  $VAA = 270^\circ$  and  $VZA = 75^\circ$ , the LKB\_T model can accurately restore it but the RTLSR model failed. Fig. 6 (a-4) and (b-4) shows that the predicted BRDF of the LKB\_T model are closer to the 1:1 line and present better consistency with the simulated BRDF, whereas a larger bias for the RTLSR model can be found. The  $R^2$  between simulated and predicted BRDF of the LKB\_T model are 0.9906 and 0.9890 in the red and NIR band, whereas those of the RTLSR model are 0.8402 and 0.6216, respectively. This suggests that the LKB\_T model can more accurately capture the distortion of BRDF shapes in the hemispheric view due to topographic effects, but the RTLSR model fails to represent this phenomenon by neglecting topographic effects and because of its intrinsic symmetry along

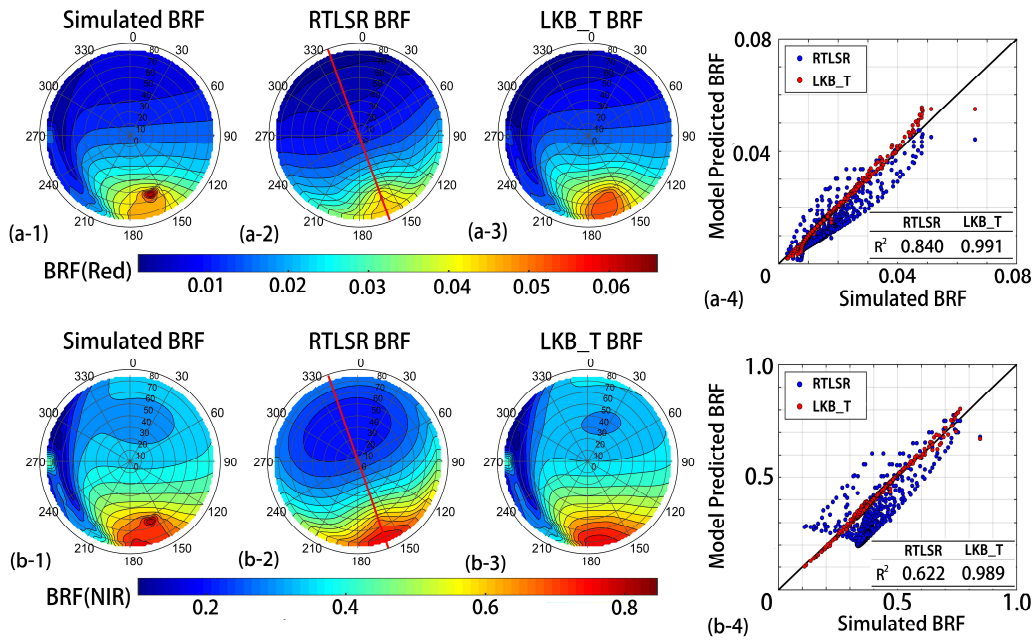


Fig. 6. Comparison of predicted BRDF shapes and accuracy in Pixel B (of Fig. 5) between the RTLSR and LKB\_T models in the red (a) and NIR (b) bands. (a-1) and (b-1) are simulated BRDF shapes of Pixel B; (a-2) and (b-2) are predicted BRDF shapes from the RTLSR model; (a-3) and (b-3) are predicted BRDF shapes from the LKB\_T model. The color bars represent BRF values. (a-4) and (b-4) compare the predicted accuracies of the RTLSR and LKB\_T models. The red lines in (a-2) and (b-2) mark the SPP.

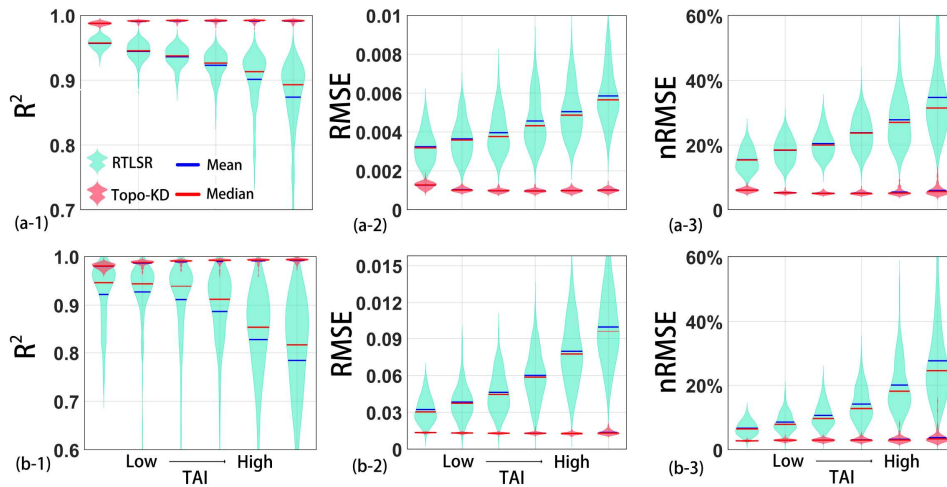


Fig. 7. Comparison of the performance of the RTLSR model and the Topo-KD algorithm in the red and NIR bands. (a-1), (a-2), and (a-3) are the  $R^2$ , RMSE, and nRMSE in the red band. (b-1), (b-2), and (b-3) are the corresponding error indicators in the NIR band. The transverse axes represent the values of TAI, and the vertical axes are the  $R^2$ , RMSE, and nRMSE values. The width of the violin plots represents the frequency of the error distribution.

the SPP.

### B. Evaluation of the Topo-KD Algorithm Based on Simulated Data

It is necessary to evaluate the Topo-KD algorithm using simulated data, we sampled simulated observations using the method shown in Fig. 4 and used Topo-KD and RTLSR to predict other directions and calculate predicted errors. The results are shown in Fig. 7 to 9.

Here, we evenly divided the 625 pixels into six TAI levels (Level 1 to 6) from small to large based on TAI (Fig. 7), to fully compare the performance of the two models over different terrains. In Fig. 7 (a-1) and (b-1), for both red and NIR bands,

the  $R^2$  of the Topo-KD are all close to 1 in all TAI levels, while the  $R^2$  of the RTLSR model gradually decrease from Level 1 to Level 6. The mean  $R^2$  of the Topo-KD in all pixels are 0.9906 and 0.9881 in the red and NIR bands, whereas those of the RTLSR model are 0.9226 and 0.8764, respectively. For the RMSE and nRMSE, the mean nRMSE of the Topo-KD algorithm are 5.5% and 3.2% in the red and NIR bands, but those for the RTLSR model are 23.5% and 14.6%. For further comparison, the ranges of nRMSE of Topo-KD are 7.8% and 13.1% in the red and NIR bands, whereas those of the RTLSR model are 75.0% and 69.1%, respectively. The RMSE and nRMSE of Topo-KD show no connection with TAI and are all

very small, but a positive correlation can be found between the RMSE and nRMSE of the RTLSR model and TAI. The above results suggest that, in both red and NIR bands, Topo-KD performs better than the RTLSR model in the study area, and the difference between the two models becomes more pronounced as the TAI increases.

The biases between simulated and predicted BRF of the RTLSR model and Topo-KD in different directions are not the same: some direction biases are large, while some are quite small (absolute bias in SPP and CPP are shown in Fig. 8). We divided all the pixels into two levels for comparison: low TAI (TAI values rank in the top 50% from small to large) and high TAI (TAI values rank in the bottom 50% from small to large).

In SPP (Fig. 8 (a-1) and (b-1)), the biases of RTLSR and Topo-KD peaks at the hotspot (VZA = -55°), this is due to the shortcomings of RTLSR in the estimation of the hotspot effect [45-47]. The Topo-KD algorithm shows larger bias at the hotspot than the RTLSR model, which should be due to the topographic correction of the LKB\_T model amplifying the deficiencies of the RTLSR kernel. In other directions in SPP, the biases of Topo-KD are smaller than those of the RTLSR model, especially when VZA is large. The biases in CPP in the red and NIR bands are given in Fig. 8 (a-2) and (b-2), showing more pronounced differences between RTLSR and Topo-KD. In the case of the RTLSR model, the biases are larger in all directions. For the red band, the percentage of mean biases of the RTLSR model in low TAI and high TAI reach 7.2% and 13.7% in CPP, whereas those of the Topo-KD are only 1.0% and 1.3%. In the NIR band, the values for the RTLSR model are 6.5% and 13.6%, while the percentage of mean biases of Topo-KD are only 0.6% and 0.7%, respectively. It is clear that the Topo-KD algorithm effectively reduces the errors in SPP and CPP compared to the RTLSR model.

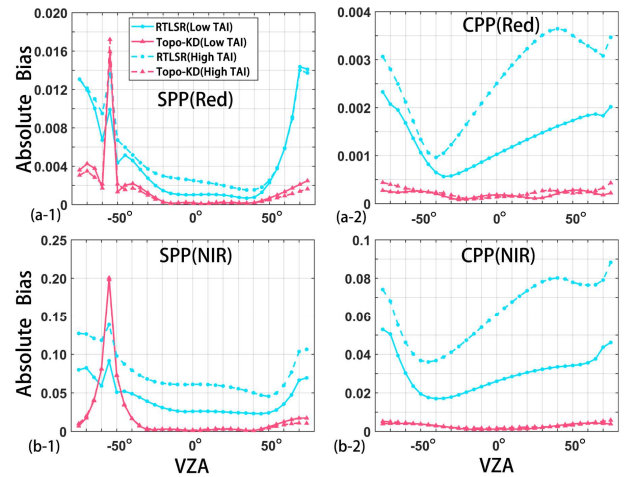


Fig.8. Absolute bias of RTLSR and Topo-KD in two special planes in the red and NIR bands. (a-1): SPP in the red band; (a-2): Cross-Principal Plane (CPP) in the red band. (b-1): SPP in the NIR band; (b-2): CPP in the NIR band.

To further investigate and compare the difference between RTLSR and Topo-KD, the mean biases between simulated and predicted BRF over the entire hemispheric view are shown in Fig. 9, again dividing all the pixels into two levels based on TAI (like Fig. 8). Overall, the polar plots of Topo-KD show a wider range of green and light blue colors in both the red and NIR bands over two types of terrain. On the contrary, the polar plots of the RTLSR model have a large proportion of dark blue and yellow regions, especially at large VZA, which means that the results of Topo-KD are closer to the simulated data across the hemispheric view. In the red band, the percentages of mean bias of the RTLSR model are 12.3% in low TAI and 19.1% in high TAI pixels, while those of Topo-KD are 2.2% and 2.3%, respectively. In the NIR band, the percentages of the RTLSR model are 7.2% in low TAI and 15.4% in high TAI pixels, while

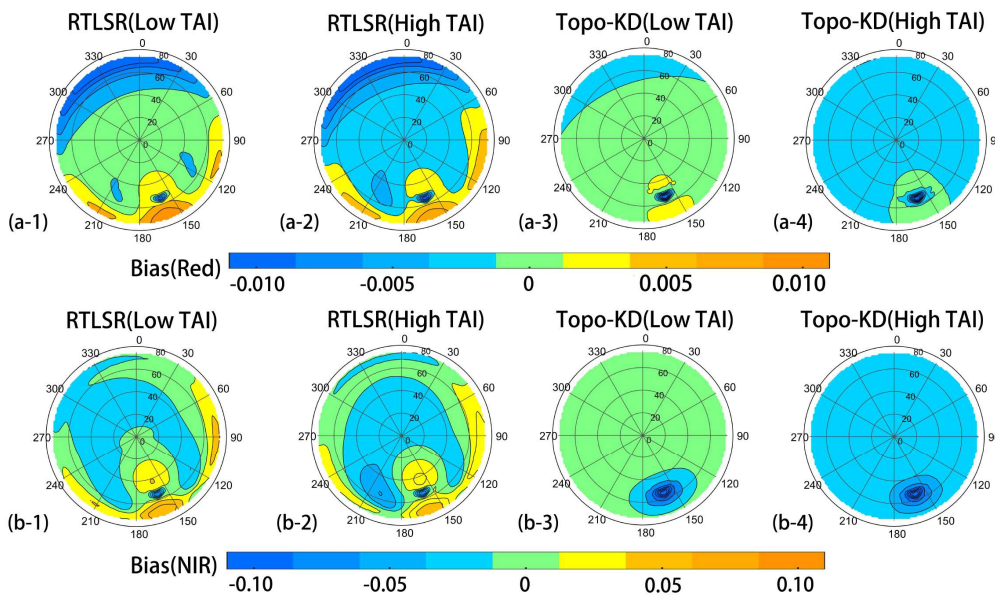


Fig. 9. Mean bias between simulated and predicted BRF from RTLSR and Topo-KD in all directions in the red (a) and NIR (b) bands. (1) and (2) are the bias of the RTLSR model in low and high TAI; (3) and (4) are the bias of the Topo-KD algorithm in low and high TAI.



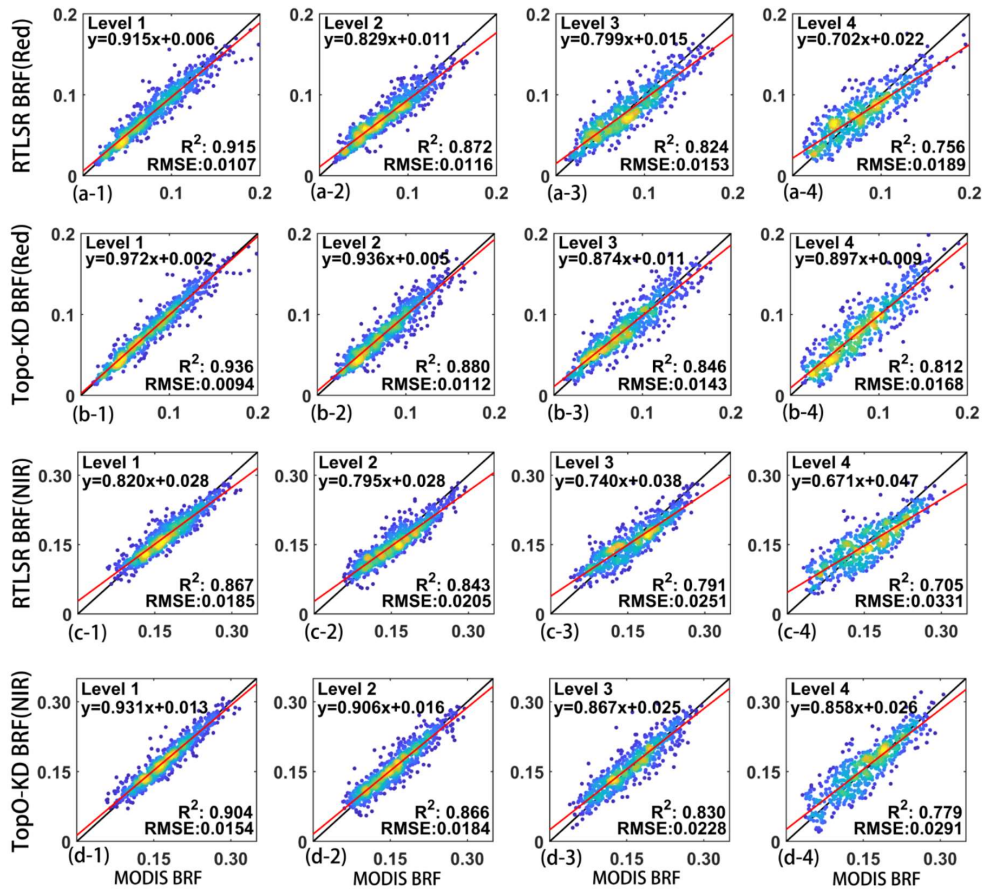


Fig. 10. Comparison of the BRF predicted by RTLSR and Topo-KD and by MODIS under different terrain in the entire study area. The red lines are the lines of best fit. The colors correspond to point density from lowest (blue) to highest (yellow). The Level 1 to 4 are the TAI levels from small to large.

those of the Topo-KD are 1.2% and 1.2%, respectively. The Topo-KD algorithm show low bias in most observation directions, except around hotspots, especially in large VZAs, the predicted accuracy is improved compared to the RTLSR model.

### C. Validation of the Topo-KD Algorithm Based on MODIS Observations

In the evaluation based on simulated data, Topo-KD show lower predicted errors compared to the RTLSR model. However, it is worth exploring whether the Topo-KD algorithm can also perform well using the real satellite data. In this section, we used the coefficients retrieved from Terra-MODIS observations to predict the Aqua-MODIS observations and evaluated the accuracy of the predictions in the entire study area. The results are shown in Fig. 10 and 11.

In Fig. 10, we divided the pixels with at least seven observations in the entire study area into four TAI levels (Level 1 to 4), from small to large. The scatterplots in Fig. 10 represent the degree of agreement between the BRF from RTLSR and Topo-KD and from MODIS observations in the red and NIR bands. The equations of the lines of best fit of the results of the RTLSR model show a gradual deviation from the 1:1 line from Level 1 to 4. Whereas the gradients of the lines of best fit of Topo-KD are all larger, which means that the predicted data are closer to the 1:1 line. In the red band (Fig. 10 (a) and (b)), the

$R^2$  of the RTLSR model decrease from 0.915 to 0.756 from Level 1 to 4, and the RMSE increase from 0.0107 to 0.0189. The  $R^2$  of Topo-KD decrease from 0.936 to 0.812, and the RMSE increase from 0.0094 to 0.0168. In the NIR band (Fig. 10 (c) and (d)), the  $R^2$  of the RTLSR model decrease from 0.867 to 0.705, and the RMSE increase from 0.0185 to 0.0331. In contrast, the  $R^2$  of Topo-KD decrease from 0.904 to 0.779, and the RMSE increase from 0.0154 to 0.0291, indicating that the results of Topo-KD are more consistent with the MODIS observations. Overall, the Topo-KD algorithm is able to reduce the predicted errors by about 10% in all terrain conditions. The errors and uncertainties in the MODIS observations lead to a small correlation between the errors of Topo-KD and TAI. After all, it is difficult to obtain ideal multi-angle BRF over rugged terrain.

Fig. 11 (b) and (c) show the distribution of fitted residuals (represented by RMSE) of the RTLSR and Topo-KD in the entire study area. In the red band, by comparing the fitting residues of the RTLSR and Topo-KD (Fig. 11 (b-1) and (b-2)), we can find that more dark blue areas are displayed in the maps of Topo-KD, which means that the overall fitting residuals are smaller; a similar pattern is also present in the NIR band. For the whole study area, the mean RMSE of Topo-KD are 0.0051 (Fig.11 (b-1)) and 0.0077 (Fig.11 (c-1)) in the red and NIR bands, whereas they are 0.0065 (Fig.11 (b-2)) and 0.0106

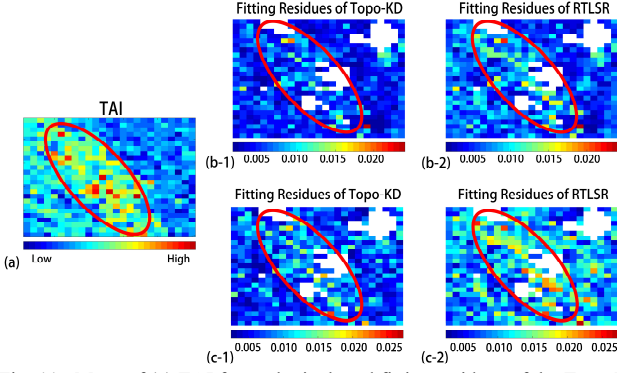


Fig. 11. Maps of (a) TAI for each pixel, and fitting residues of the Topo-KD algorithm and the RTLSR model in the (b) red and (c) NIR bands. (1) are the fitting residuals of Topo-KD and (2) are the residuals for RTLSR. The red solid ellipses mark a prominent area.

(Fig.11 (c-2)) for the RTLSR model, respectively. The Topo-KD algorithm reduces errors in the red and NIR bands by 21.5% and 27.4%, which indicate that Topo-KD can provide more accurate land surface reflectance data for the retrieval of other parameters. There is a positive correlation between the fitting residuals of the RTLSR model and the TAI values as shown in Fig. 11 (a), (b-2) and (c-2), especially in the area enclosed by the red ellipse. However, this phenomenon is improved in the map of the Topo-KD algorithm. In some pixels, Topo-KD and RTLSR both show poor fitting accuracy, which may be caused by noise in the measurements, errors in the data, and imperfect model assumptions. At the same time, the distribution of the observation angles also affects the retrieved accuracy (see Discussion Section A.).

#### IV. DISCUSSION

##### A. Sensitivity to the Distribution of Observations

We believe that if the distribution of the observation angles is not uniform enough, the RTLSR model and the Topo-KD algorithm cannot describe the bidirectional reflection of the surface well. So, we used simulated data and three sampling methods (Method A, B, and C) to validate the influence of the distribution of observation angle on fitting accuracy of the models.

The three sampling methods are shown in Fig. 12 (a): Method A: The sampling angle is concentrated within  $0^\circ$ - $90^\circ$  azimuth; Method B: The sampling angle is distributed within  $0^\circ$ - $180^\circ$  azimuth; Method C: its observation angles are uniformly distributed in the whole hemispherical space. All methods used 16 angles for retrieval but with different distributions of their sampling angles. Fig. 12 (b-1) and (b-2) show the RMSE and standard deviation (error bars) of the RTLSR and Topo-KD models over low and high TAI terrains when three different methods are used in the red and NIR bands. For the red band in low TAI, the RMSE of Method A for the RTLSR model reaches the maximum value, and Methods B and C decrease sequentially, their standard deviation are similar. In high TAI pixels in the red band, there is the same trend in the two models. But the difference is that the RMSE and standard deviation of the methods all become larger, especially for the RTLSR model. These suggest that it will result in larger errors when the distribution of observations is concentrated, which leads to a

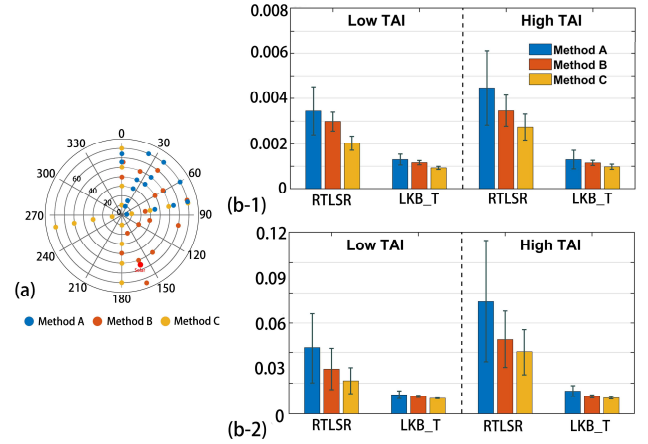


Fig. 12. Three angle sampling methods and their predicted error. (a): angles distribution of three sampling methods; (b-1) the RMSE of three methods in the red band; (b-2) the RMSE of three methods in the NIR band. Error bars represent the standard deviation.

decrease of the retrieved accuracy for both RTLSR and Topo-KD models. Moreover, this effect is exacerbated in rugged terrain. The trend is similar in the NIR band. Due to the difficulties of obtaining high-quality observations over rugged terrain, the distribution of available observations from a single sensor may be concentrated in certain directions after quality control, which has been addressed by Wen et al. with a multisensor combined BRDF inversion model. [48].

##### B. Accuracy and efficiency evaluation of the Topo-KD algorithm

For applications of the Topo-KD algorithm, accuracy optimization and computational efficiency are important indicators and are also of interest to users. We analyzed and discussed the accuracy optimization and computing efficiency of the Topo-KD algorithm using simulated data. In this section, we did not consider the inversion results around the hotspot because of the shortcomings of the RTLSR kernels about the hotspot. We describe the accuracy optimization level with the following equation:

$$\frac{B}{A} = \frac{bias_A - bias_B}{bias_A} \times 100\% \quad (8)$$

where  $bias_A$  is the absolute bias between the simulated and retrieved BRFs from model A, which was mentioned in Equation (7).

In Fig. 13 (a), Topo-KD(n) means that n time adjacent terrain-reflected radiances are considered by the Topo-KD algorithm. Compared to the RTLSR model, the mean optimization rate of Topo-KD(0) can reach 80.12% and 85.43% in the red and NIR bands. The mean optimization rate of Topo-KD(1) compared to Topo-KD(0) can reach 20.18% and 37.22% in the red and NIR bands. This means that, after considering the reflected radiation from adjacent terrain, the accuracy of the Topo-KD algorithm can be improved by more than 20%. The optimization rate is higher in the NIR band, which should be due to that the multi-scattering within the canopy is larger in the



NIR band and the adjacent topographic radiation is more pronounced.

In Fig. 13 (b), we compare the run time of the Topo-KD algorithm using simulated data to retrieve the entire study area compared to the RTLSR model. When dividing all pixels into rugged pixels, Topo-KD(1) and Topo-KD(0) take 4.4 and 3.1 times longer, respectively, compared to the RTLSR model. When the terrain indexes are adjusted to divide 25% of the pixels into rugged pixels, Topo-KD(1) and Topo-KD(0) take 1.8 and 1.5 times longer, respectively. The reduction in their running times implies that the pixel classification using the terrain index threshold is effective in improving the computational efficiency of the Topo-KD algorithm.

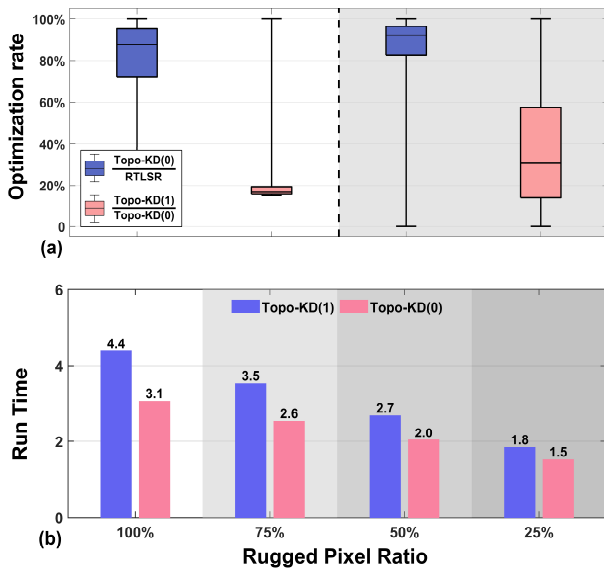


Fig. 13. Comparison of the accuracy optimization and computational efficiency for the Topo-KD algorithm. Topo-KD(n) means that n time adjacent terrain-reflected radiances are considered. Panel (a) show the accuracy optimization of the Topo-KD algorithm. White and gray backgrounds represent the red and NIR bands. (b) is the comparison of run time used by the Topo-KD model to retrieve the entire study area using simulated data in different pixel classifications, its vertical axis represents multiples of RTLSR running times.

### C. Algorithm Advantages and Applications

Global ecological and environmental monitoring relies on accurate estimates of land surface variables and biological parameters (such as albedo and LAI) over mountainous areas [17]. However, it is difficult to obtain high-quality reflectance data for areas with a complex terrain. Previous studies have reported that rugged terrain greatly influences BRDF modeling [20, 49, 50], and in our results, we also can see that the BRDF shape of the pixel can be affected by the terrain (Fig. 5). But none of the existing models can be used operationally to fit satellite multi-angular reflectance and model BRDF because of their neglect of multiple-scattering effects between subpixel terrains and complexity [17].

The Topo-KD algorithm presents several advantages in more rigorously modeling rugged terrain. First, the LKB\_T model combines the RLKB and MRT models, uses a high-resolution DEM to correct illumination and viewing geometry, and takes

into account the reflected radiation from adjacent terrain. This makes Topo-KD can better describe the RT process over rugged terrain areas. And compared with other existing models such as TCKD [25], the Topo-KD algorithm performs a better fitting accuracy. This should because of the consideration of multiple-scattering effects in its kernel model LKB\_T and the avoidance of Taylor expansion approximation. Second, the linear forms of the RLKB models are retained, which allows the Topo-KD algorithm can couple with other kernel functions. A new LUT should be used to store all the required parameters to further improve its calculation efficiency. Third, the Topo-KD algorithm allows users to adjust the terrain thresholds ST and TT settings so that they can trade-off between accuracy and efficiency according to the situation.

The Topo-KD algorithm can be used to fit satellite multi-angular reflectance and model BRDF to participate in the retrieval and estimation of other parameters. For example, the coefficients from the Topo-KD algorithm can reflect the canopy density on the land surface. Thus, Topo-KD can also be used to retrieve canopy structure parameters such as LAI from the coefficients like the RLKB models. Besides, the three “generalized-kernels” of the LKB\_T model, which are functions of both sun-sensor geometry and terrain factors, allow it to be used to estimate albedos in conjunction with a LUT of pre-computed kernel integrals, but the traditional LUT of kernel integrals needs to be replaced by a more complex table. Based on an assumption that terrain remains constant over a period of time, these factors can be calculated in advance and used repeatedly. Therefore, Topo-KD can also be used to estimate spectral albedos by building such a LUT. So, we believe that the Topo-KD algorithm is a good choice to model BRDF in rugged areas, and it also provides the ability to better estimate the surface albedo and LAI.

Currently, many operational BRDF/Albedo algorithms use the RLKB model which does not explicitly consider terrain to produce global products. The Topo-KD algorithm is designed as an extension of the kernel-driven model, retaining the easy-retrieval linear form. It can also improve the retrieval accuracy over rugged terrain with guaranteed computational efficiency and ensure product consistency. Therefore, we think that Topo-KD has the potential to be used as an operational algorithm for producing global products after more validations and optimization in future work.

### D. Limitations and Future Work

The construction and validation of the Topo-KD algorithm still presents some challenges. First, the Topo-KD algorithm needs a high-quality DEM to describe the terrain, which inevitably introduce more input data uncertainty. This may make the LKB\_T exhibit similar or even larger output uncertainty than RTLSR when satellite observations with poor-quality are used. Therefore, to improve the reliability of the results we compared the results of LKB\_T with those of RTLSR in the Topo-KD algorithm and selected the one with a smaller error. Second, it remains difficult to obtain ideal reflectance data due to the high frequency of cloudiness over rugged terrain [46]. Although we have eliminated some poor-

quality data through quality control, cloud detection screening algorithms never work perfectly and residual clouds may contaminate the remaining observations flagged as cloud-free. Third, 30 days of multi-angle observation data were used in this study to ensure enough observations, but the BRDF characteristics of the study area may change during this period, which can affect the validation results. Finally, the range of TAI varies with the number of DEM pixels within a coarse pixel, so users do not have a good reference standard when using this index for pixel classification. In future work, we will optimize this terrain index and provide a TAI reference value for pixel classification.

This paper focused on construction and preliminary analysis of the algorithm. Future work will include sensitivity analysis and additional validation of the Topo-KD algorithm. We will conduct an on-site validation to better understand the performance of the algorithm and reduces uncertainty of satellite data. With the improvement of sand-table technologies and the introduction of three-dimensional printing, a ground-based multi-angle observation device [51] can be combined with miniature topographical models based on real DEM. We also can obtain high-quality DEM data from field measurements to avoid geo-registration errors. After more comprehensive validations and analysis of the Topo-KD algorithm, we will further improve its computational efficiency and reliability. Moreover, some recent research advances for single-slope BRDF modeling [16, 52] can also be used to improve the accuracy of our Topo-KD algorithm.

## V. CONCLUDING REMARKS

The RLKB models are widely used to retrieve the bidirectional reflectance of the land surface but do not explicitly include the influence of terrain. In this paper, we addressed this limitation by proposing a hybrid algorithm, Topo-KD, which combines the traditional RLKB model with our more explicit LKB\_T model. By using RTLSR kernel, simulated data from the SAILH model and multi-angular observations data were employed to compare the fitting ability of the Topo-KD algorithm and the RTLSR model in rugged terrain. The conclusions are as follows:

- 1) Rugged terrain causes variability in the BRDF shape of the pixel. The RTLSR model cannot accurately describe the BRDF characteristics of a rugged pixel because of its inherent symmetric kernel, whereas the LKB\_T shows a better performance.
- 2) In algorithm evaluation and validation, Topo-KD shows consistently lower errors than RTLSR. Based on the simulated data, the mean  $nRMSE$  of Topo-KD are 5.5% and 3.2% in the red and NIR bands, and those for the RTLSR model are 23.5% and 14.6%. Against satellite observations data, the mean  $RMSE$  of Topo-KD are 0.0051 and 0.0077 in the red and NIR bands, whereas the mean  $RMSE$  of the RTLSR model are 0.0065 and 0.0106, respectively. The Topo-KD algorithm reduces errors in the red and NIR bands by 21.5% and 27.4%.
- 3) The difference between Topo-KD and RTLSR depends on the terrain: the advantages of the Topo-KD algorithm are

more pronounced over extremely rugged terrain. According to the algorithm evaluation based on the simulated data, the mean  $nRMSE$  of Topo-KD in low and high TAI pixels are 6.1% and 6.0% in the red band, whereas those of the RTLSR model reach 15.5% and 34.7%, respectively. In the NIR band, the mean  $nRMSE$  of Topo-KD are 2.8% and 3.8%, and those of the RTLSR model are 6.7% and 27.6%, respectively. These trends are similar in the algorithm validation.

The Topo-KD algorithm explicitly considers the topographic effects which can provide a more detailed description of multiple-scattering between adjacent mountains, improving the accuracy of retrieval on rugged terrain, and it inherits the advantages of the RLKB models. We think it can be a better choice in BRDF modeling for rugged areas and have potential as a new operational algorithm after more validations and analysis.

## APPENDIX

## A. Nomenclature

Label	Description	Label	Description
<b>Topography and geometric variables</b>			
$\theta_s, \varphi_s$ and $\theta_v, \varphi_v$	Sun-sensor geometry (solar zenith and azimuth angles, view zenith and azimuth angles)	$E_{sun\_h}, E_{sky\_h}$	Direct solar and hemispherical sky diffused irradiance on a horizontal plane at the bottom of atmosphere
$\varphi$	Relative azimuth angle	$E_{sun\_s}, E_{sky\_s}$	Direct solar and hemispherical sky diffused irradiance on a slope
$S, A$	Slop angle and aspect	$E_{ref}$	Adjacent-terrain reflected irradiance on a slope
$i$	The angle between the incident ray and the slope surface normal	$L_p$	Energy received by surrounding slopes
$\mu_s, \mu_v$	Projection coefficients of solar and view direction respectively	$k, K$	Fraction of diffused sky irradiance and fraction of terrain-reflected irradiance
$\Theta_s, \Theta_v$	Shelter indicators of solar and view direction, 0 or 1	<b>Reflectance and spectral variables</b>	
$V_d$	The sky view factor, between 0 and 1	$R$	Bidirectional reflectance of a coarse pixel
$\theta'_s, \theta'_v$	Equivalent solar and view zenith angle	$\lambda$	Spectral band
$\varphi'_s, \varphi'_v$	Equivalent solar and view azimuth angles	$BRDF_{i,j}$	Directional-directional reflectance of the slope (i, j)
$T_M$	The angle between the line from surrounding slope to target slope and the normal of surrounding slope	$HDR_{i,j}, DHR_{i,j}$	Hemispheric-directional and directional-hemispheric reflectance of the slope (i, j)
$T_P$	The angle between the line from surrounding slope to target slope and the normal of the target slope	$k_{vol}, k_{geo}$	BRDF kernels of volume scattering and geometric optical scattering
$dS_p$	The area of the target slope	$h'_{vol}, h'_{geo}$	HDR kernels of volume scattering and geometric optical scattering
$r_{MP}$	The length from surrounding slope to target slope	$h_{vol}, h_{geo}$	DHR kernels of volume scattering and geometric optical scattering
$n$	Number of DEM lines or samples in a coarse pixel	$ker^{local}$	Local kernel function of a single slop
$\Theta$	Shelter indicator between surrounding slope and target slope, 0 or 1	$ker^l$	Redefined kernel function of a coarse pixel, named as "generalized-kernels"
<b>Radiation variables</b>		$f_{so}, f_{vol}$ and $f_{geo}$	Weight coefficients of kernels

## B. Mountain Radiative Transfer Model

The adverse topographic effects in a pixel's directional reflectance mainly lie in six aspects (Fig. A1): 1) slope impacts incident radiation; 2) some slopes cannot receive direct solar radiation because it is blocked by the surrounding slopes; 3) some of the sky-diffused radiation is obstructed by surrounding slopes; 4) adjacent terrain reflects the radiation to the target slope; 5) some slopes cannot be seen by the sensor because of the overlap of surrounding slopes or the so-called mountain-block effect; and 6) local sun-sensor geometry on each slope varies and each slope's BRDF rotates with the equivalent geometry.

## 1) Direct solar radiation

As shown in Fig. A1 (a), topography causes a change in illumination geometry and the direct solar irradiance on a slope can be expressed as:

$$E_{sun\_s} = \cos(i_s) \times E_{sun\_h} / \cos \theta_s \quad (A1)$$

where  $E_{sun\_h}$  is the direct solar irradiance of a horizontal plane at the bottom of the atmosphere;  $i_s$  is the angle between the incident ray and the slope surface normal; this angle is a function of slope  $S$ , aspect  $A$ , incident zenith  $\theta_s$  and azimuth angles  $\varphi_s$ , and can be expressed as:

$$\mu_s = \cos(i_s) = \cos \theta_s \cos S + \sin \theta_s \sin S \cos(\varphi_s - A) \quad (A2)$$

Moreover, some slopes may be sheltered by surrounding slopes, meaning that the target slope may "fall" into the surrounding slopes' shadows and be unable to receive direct radiation from the sun (Fig. A1 (b)). We thus define a Boolean shadow coefficient  $\Theta_s$  to represent whether the target slope can receive direct solar radiation. If the solar position and DEM are known, we can then obtain the incident direct solar irradiance of each slope. Equation (A1) can be further expressed as follows:

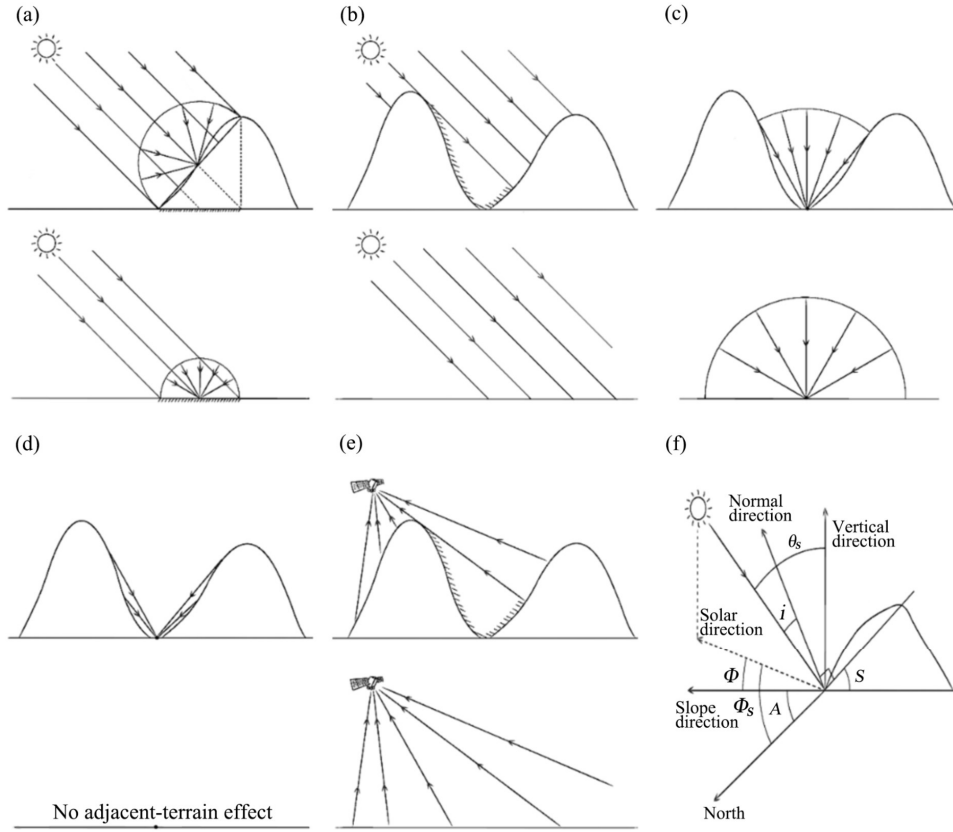


Fig. A1. Six aspects of topographic effects on directional reflectance compared with a flat surface. In each panel, the upper part of each drawing shows the effect of topography and the lower part shows the effect on a flat surface. Panel (f) shows the local sun-sensor geometry.

$$E_{sun\_s} = \Theta_s \times \mu_s \times E_{sun\_h} / \cos \theta_s \quad (A3)$$

## 2) Sky diffused radiation

In this paper, we adopted Dozier's method to calculate sky diffused radiation (Dozier and Frew 1990). The diffused solar irradiance on the slope can be expressed as (see Fig. A1 (c)):

$$E_{sky\_s} = V_d E_{sky\_h} \quad (A4)$$

where the sky view factor  $V_d$  is introduced as the ratio of sky diffuse scattering received on a slope to that on an unobstructed horizontal surface. Depending on the extent of the terrain shade, the sky view factor varies between 0 (minimum terrain shade) and 1 (maximum terrain shade).  $E_{sky\_h}$  is the hemispherical sky diffused irradiance at the bottom of the atmosphere.

## 3) Adjacent-terrain reflected radiation

The adjacent-terrain reflected radiation (see Fig. A2 (d)) is obtained through the method established by Proy et al. [15]. Assuming the surface of the subpixel is Lambertian, this method is applied with a filter with a 5 by 5 pixels matrix with subpixel M located in the center of the matrix, and subpixel Ps neighboring M. The reflected irradiation comes from each surrounding point P to M and can be calculated point-by-point from:

$$E_{ref} = \sum_{P=1}^N \left( \frac{\Theta L_P \cos T_M \cos T_P dS_P}{r_{MP}^2} \right) \quad (A5)$$

where  $L_P$  is the energy received by the surrounding slopes,  $T_M$  is the angle between the line from surrounding slope to target slope and the normal of each surrounding slope,  $T_P$  is the angle between the line from surrounding slope to target slope and the normal of the target slope,  $dS_P$  is the area of the target slope,  $r_{MP}$  is the length from surrounding slope to target slope.  $\Theta$  is 1 if the surrounding slope and target slope are unobstructed, otherwise it is 0. As with the definition of sky view factor, we defined the terrain-reflected irradiance factor as:

$$K = \frac{E_{ref}}{E_{sun\_h}} \quad (A6)$$

## 4) Local sun-sensor geometry

Topography does not only affect the received radiation; it can also change the observation geometry. We thus need to switch the coarse pixel's sun-sensor geometry to an equivalent geometry under the local coordinate system of each slope. As Fig. A1 (f) shows, the transfer formula is:

$$\begin{aligned} \cos \theta'_{s,v} &= \cos \theta_{s,v} \cos S + \sin \theta_{s,v} \sin S \cos(\varphi_{s,v} - A) \\ \tan \phi'_{s,v} &= \frac{\sin(\phi_{s,v} - A) \sin \theta_{s,v}}{\sin \theta_{s,v} \cos S \cos(\phi_{s,v} - A) - \cos \theta_{s,v} \sin S} \end{aligned} \quad (A7)$$

where  $\theta'_s$  and  $\theta'_v$  represent the equivalent solar and view zenith angle;  $\phi'_s$  and  $\phi'_v$  represent the equivalent solar and

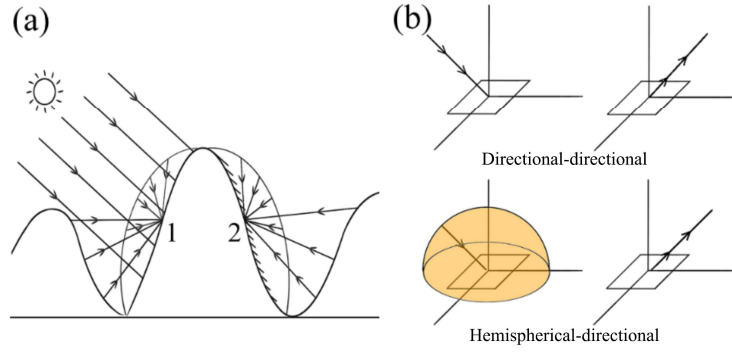


Fig. A2. Difference between incoming radiation of sunlit and shaded slopes (a) shows three sources on sunlit slope 1 and only two sources on shaded slope 2; (b) shows two kinds of directional reflectance-BRDF and HDR).

view azimuth angle.

##### 5) Bidirectional reflectance of the coarse pixel

The coarse pixel's bidirectional reflectance, which is affected by subpixel topography, is defined as the ratio of the reflected radiation by sensor-visible area to the received radiation of that area. The slopes that can be seen by the sensor are divided into two categories: sunlit and shaded (Fig. 2 (a)). In rugged areas, the components of downward radiation on a sunlit slope come from three different sources: (1) direct solar radiance not scattered by the atmosphere; (2) sky diffused radiance; and (3) adjacent-terrain-reflected radiance. The shaded slope cannot

receive direct solar radiance. As previous studies have shown, the surface reflectance for direct solar radiance is a directional-directional reflectance (BRDF), while the surface reflectance for sky diffuse radiance and terrain-reflected radiance is more like a hemispheric-directional reflectance (HDR) (Fig. 2 (b)). The low-resolution pixel's bidirectional reflectance  $R(\theta_s, \varphi_s, \theta_v, \varphi_v, DEM)$  can be written as (A8), where  $\mathcal{Q}_v$  and  $\mathcal{Q}_s$  indicate whether the slope is visible by the sensor and whether the slope is sunlit, respectively;  $k$  is the fraction of diffused illumination.

$$R = \frac{\sum_{i=1}^n \sum_{j=1}^n \{\mathcal{Q}_{v_{i,j}} \mu_{v_{i,j}} / \cos(S_{i,j}) \times [BRDF_{i,j} \Theta_{s_{i,j}} \mu_{s_{i,j}} + HDR_{i,j} (kVd_{i,j} + K_{i,j})]\}}{[\cos(\theta_s) + k] \sum_{i=1}^n \sum_{j=1}^n [\mathcal{Q}_{v_{i,j}} \mu_{v_{i,j}} / \cos(S_{i,j})]} \quad (A8)$$

## REFERENCES

- [1] J. Roujean, M. Leroy, P. Y. Deschamps, and A. Podaire, "A Surface Bidirectional Reflectance Model To Be Used For The Correction Of Directional Effects In Remote Sensing Multitemporal Data Sets," in *international geoscience and remote sensing symposium*, 1990, pp. 1785-1789.
- [2] J. Roujean, M. Leroy, A. Podaire, and P. Y. Deschamps, "Evidence of surface reflectance bidirectional effects from a NOAA/ AVHRR multi-temporal data set," *International Journal of Remote Sensing*, vol. 13, no. 4, pp. 685-698, 1992.
- [3] Z. Li, J. Cihlar, X. Zheng, L. Moreau, and H. Ly, "The bidirectional effects of AVHRR measurements over boreal regions," *IEEE Transactions on Geoscience and Remote Sensing*, vol. 34, no. 6, pp. 1308-1322, 1996.
- [4] A. Berk *et al.*, "MODTRAN4 radiative transfer modeling for atmospheric correction," in *Optical Spectroscopic Techniques and Instrumentation for Atmospheric and Space Research Iii*, vol. 3756, A. M. Larar, Ed. (Proceedings of the Society of Photo-Optical Instrumentation Engineers (Spie), 1999, pp. 348-353.
- [5] E. Vermote, D. Tanre, J. L. Deuze, M. Herman, and J. J. Morcette, "Second Simulation of the Satellite Signal in the Solar Spectrum, 6S: an overview," *IEEE Transactions on Geoscience and Remote Sensing*, vol. 35, no. 3, pp. 675-686, 1997.
- [6] R. E. Dickson, "LAND PROCESSES IN CLIMATE MODELS," *Remote Sensing of Environment*, vol. 51, no. 1, pp. 27-38, Jan 1995.
- [7] W. Lucht, C. B. Schaaf, and A. H. Strahler, "An algorithm for the retrieval of albedo from space using semiempirical BRDF models," *IEEE Transactions on Geoscience and Remote Sensing*, vol. 38, no. 2, pp. 977-998, 2000.
- [8] O. S. Pokrovsky and J. Roujean, "Land surface albedo retrieval via kernel-based BRDF modeling: I. Statistical inversion method and model comparison," *Remote Sensing of Environment*, vol. 84, no. 1, pp. 100-119, 2003.
- [9] M. Matsuoka *et al.*, "Bidirectional reflectance modeling of the geostationary sensor HIMAWARI-8/AHI using a Kernel-driven BRDF model," *ISPRS Annals of the Photogrammetry, Remote Sensing and Spatial Information Sciences*, vol. 3, p. 3, 2016.
- [10] J. Wen, Q. Liu, Q. Liu, Q. Xiao, and X. Li, *Scale effects and correction for land surface albedo in rugged terrain* (Proceedings of the 8th International Symposium on Spatial Accuracy Assessment in Natural Resources and Environmental Sciences, Vol I: Spatial Uncertainty). 2008, pp. 167-175.
- [11] S. Wu *et al.*, "Derivation of Kernel functions for Kernel-driven reflectance model over sloping terrain," *IEEE Journal of Selected Topics in Applied Earth Observations and Remote Sensing*, vol. 12, no. 2, pp. 396-409, 2018.
- [12] D. Hao, J. Wen, Q. Xiao, S. Wu, and J. Cheng, "An improved Kernel-driven BRDF model coupled with topography: KDCT," in *IGARSS 2018-2018 IEEE International Geoscience and Remote Sensing Symposium*, 2018: IEEE, pp. 3959-3962.
- [13] D. Hao *et al.*, "Simulation and analysis of the topographic effects on snow-free albedo over rugged terrain," *Remote Sensing*, vol. 10, no. 2, p. 278, 2018.
- [14] A. Mousivand, W. Verhoef, M. Menenti, and B. Gorte, "Modeling top of atmosphere radiance over heterogeneous non-Lambertian rugged terrain," *Remote sensing*, vol. 7, no. 6, pp. 8019-8044, 2015.
- [15] C. Proy, D. Tanre, and P. Deschamps, "Evaluation of topographic effects in remotely sensed data," *Remote Sensing of Environment*, vol. 30, no. 1, pp. 21-32, 1989.
- [16] S. Wu *et al.*, "The definition of remotely sensed reflectance quantities suitable for rugged terrain," *Remote sensing of environment*, vol. 225, pp. 403-415, 2019.
- [17] J. Wen *et al.*, "Characterizing land surface anisotropic reflectance over rugged terrain: A review of concepts and recent developments," *Remote Sensing*, vol. 10, no. 3, p. 370, 2018.
- [18] X. Li and A. H. Strahler, "Geometric-optical bidirectional reflectance modeling of the discrete crown vegetation canopy: effect of crown shape and mutual shading," *IEEE Transactions on Geoscience and Remote Sensing*, vol. 30, no. 2, pp. 276-292, 1992.
- [19] C. B. Schaaf, X. Li, and A. H. Strahler, "Topographic effects on bidirectional and hemispherical reflectances calculated with a geometric-optical canopy model," *IEEE Transactions on Geoscience and Remote Sensing*, vol. 32, no. 6, pp. 1186-1193, 1994.
- [20] G. Yin, A. Li, W. Zhao, H. Jin, J. Bian, and S. Wu, "Modeling canopy reflectance over sloping terrain based on path length correction," *IEEE Transactions on Geoscience and Remote Sensing*, vol. 55, no. 8, pp. 4597-4609, 2017.
- [21] S. Liang, *Quantitative remote sensing of land surfaces*. John Wiley & Sons, 2005.
- [22] S. Sandmeier and K. I. Itten, "A physically-based model to correct atmospheric and illumination effects in optical satellite data of rugged terrain," *IEEE Transactions on Geoscience and Remote Sensing*, vol. 35, no. 3, pp. 708-717, 1997.
- [23] J. D. Shepherd and J. R. Dymond, "Correcting satellite imagery for the variance of reflectance and illumination with topography," *International Journal of Remote Sensing*, vol. 24, no. 17, pp. 3503-3514, 2003.
- [24] D. Hao *et al.*, "Modeling anisotropic reflectance over composite sloping terrain," *IEEE Transactions on Geoscience and Remote Sensing*, vol. 56, no. 7, pp. 3903-3923, 2018.
- [25] D. Hao, J. Wen, Q. Xiao, D. You, and Y. Tang, "An Improved Topography-Coupled Kernel-Driven Model for Land Surface Anisotropic Reflectance," *IEEE Transactions on Geoscience and Remote Sensing*, vol. 58, no. 4, pp. 2833-2847, 2019.
- [26] J. Ross, *The radiation regime and architecture of plant stands*. Springer Science & Business Media, 1981.
- [27] W. Wanner, X. Li, and A. H. Strahler, "On the derivation of kernels for kernel-driven models of bidirectional reflectance," *Journal of Geophysical Research*, vol. 100, pp. 21077-21089, 1995.
- [28] W. Lucht and J. L. Roujean, "Considerations in the parametric modeling of BRDF and albedo from multiangular satellite sensor observations," *Remote Sensing Reviews*, vol. 18, no. 2-4, pp. 343-379, 2000.
- [29] C. B. Schaaf *et al.*, "First operational BRDF, albedo nadir reflectance products from MODIS," *Remote Sensing of Environment*, vol. 83, no. 1, pp. 135-148, 2002.
- [30] C. Schaaf, J. Liu, F. Gao, and A. H. Strahler, "MODIS albedo and reflectance anisotropy products from Aqua and Terra," *Land Remote Sensing and Global Environmental Change: NASA's Earth Observing System and the Science of ASTER and MODIS*, vol. 11, pp. 549-561, 2011.
- [31] Z. Wang, C. B. Schaaf, Q. Sun, Y. Shuai, and M. O. Román, "Capturing rapid land surface dynamics with Collection V006 MODIS BRDF/NBAR/Albedo (MCD43) products," *Remote Sensing of Environment*, vol. 207, pp. 50-64, 2018.
- [32] R. E. Wolfe, D. P. Roy, and E. Vermote, "MODIS land data storage, gridding, and compositing methodology: Level 2 grid," *IEEE Transactions on Geoscience and Remote Sensing*, vol. 36, no. 4, pp. 1324-1338, 1998.
- [33] M. L. Campagnolo and E. L. Montano, "Estimation of effective resolution for daily MODIS gridded surface reflectance products," *IEEE Transactions on Geoscience and Remote Sensing*, vol. 52, no. 9, pp. 5622-5632, 2014.
- [34] A. Souiri and A. Azizi, "Removing Bowtie phenomenon by correction of panoramic effect in MODIS imagery," *International Journal of Computer Applications*, vol. 68, no. 3, 2013.
- [35] J. L. Privette, T. F. Eck, and D. W. Deering, "Estimating spectral albedo and nadir reflectance through inversion of simple BRDF models with AVHRR/MODIS-like data," *Journal of Geophysical Research*, vol. 102, pp. 29529-29542, 1997.
- [36] W. Wanner *et al.*, "Global retrieval of bidirectional reflectance and albedo over land from EOS MODIS and MISR data: Theory and algorithm," *Journal of Geophysical Research*, vol. 102, pp. 17143-17161, 1997.
- [37] A. Hirano, R. Welch, and H. Lang, "Mapping from ASTER stereo image data: DEM validation and accuracy assessment," *Isprs Journal of Photogrammetry and Remote Sensing*, vol. 57, no. 5, pp. 356-370, 2003.
- [38] B. Gao, L. Jia, and M. Menenti, "The retrieval of land surface albedo in rugged terrain," in *international workshop on earth observation and remote sensing applications*, 2012, pp. 41-45.
- [39] Y. Deng, J. P. Wilson, and B. Bauer, "DEM resolution dependencies of terrain attributes across a landscape," *International Journal of Geographical Information Science*, vol. 21, no. 2, pp. 187-213, 2007.
- [40] G. Schaepmanstrub, M. E. Schaepman, T. H. Painter, S. Dangel, and J. Martonchik, "Reflectance quantities in optical remote sensing—



- definitions and case studies," *Remote Sensing of Environment*, vol. 103, no. 1, pp. 27-42, 2006.
- [41] J. Dozier and J. Frew, "RAPID CALCULATION OF TERRAIN PARAMETERS FOR RADIATION MODELING FROM DIGITAL ELEVATION DATA," *Ieee Transactions on Geoscience and Remote Sensing*, vol. 28, no. 5, pp. 963-969, Sep 1990.
- [42] S. Liang *et al.*, "Validating MODIS land surface reflectance and albedo products: methods and preliminary results," *Remote Sensing of Environment*, vol. 83, no. 1, pp. 149-162, 2002.
- [43] J. T. Morisette, J. L. Privette, and C. O. Justice, "A framework for the validation of MODIS Land products," *Remote Sensing of Environment*, vol. 83, no. 1, pp. 77-96, 2002.
- [44] A. Kuusk, *THE HOT-SPOT EFFECT IN THE LEAF CANOPY* (Igarss 91 - Remote Sensing : Global Monitoring for Earth Management, Vols 1-4). 1991, pp. 1555-1557.
- [45] J. Chen and J. Cihlar, "A hotspot function in a simple bidirectional reflectance model for satellite applications," *Journal of Geophysical Research: Atmospheres*, vol. 102, no. D22, pp. 25907-25913, 1997.
- [46] F. Maignan, F.-M. Bréon, and R. Lacaze, "Bidirectional reflectance of Earth targets: Evaluation of analytical models using a large set of spaceborne measurements with emphasis on the Hot Spot," *Remote Sensing of Environment*, vol. 90, no. 2, pp. 210-220, 2004.
- [47] Z. Jiao *et al.*, "A method for improving hotspot directional signatures in BRDF models used for MODIS," *Remote Sensing of Environment*, vol. 186, pp. 135-151, 2016.
- [48] J. Wen *et al.*, "Forward a small-timescale BRDF/Albedo by multisensor combined brdf inversion model," *IEEE Transactions on Geoscience and Remote Sensing*, vol. 55, no. 2, pp. 683-697, 2016.
- [49] F. Li *et al.*, "A physics-based atmospheric and BRDF correction for Landsat data over mountainous terrain," *Remote Sensing of Environment*, vol. 124, pp. 756-770, 2012.
- [50] J. Wen *et al.*, "Modeling land surface reflectance coupled BRDF for HJ-1/CCD data of rugged terrain in Heihe river basin, China," *IEEE Journal of Selected Topics in Applied Earth Observations and Remote Sensing*, vol. 8, no. 4, pp. 1506-1518, 2015.
- [51] G. Yan, H. Ren, R. Hu, K. Yan, and W. Zhang, "A portable Multi-Angle Observation System," in *international geoscience and remote sensing symposium*, 2012, pp. 6916-6919.
- [52] S. Wu, J. Wen, Q. Liu, D. You, G. Yin, and X. Lin, "Improving Kernel-Driven BRDF Model for Capturing Vegetation Canopy Reflectance With Large Leaf Inclinations," *IEEE Journal of Selected Topics in Applied Earth Observations and Remote Sensing*, vol. 13, pp. 2639-2655, 2020.



**Kai Yan** received the B.S. degree in mapping and surveying from the Beijing University of Civil Engineering and Architecture, Beijing, China, in 2011, and the Ph.D. degree in GIS/RS from Beijing Normal University, Beijing, in 2018.

He was a Visiting Scholar with the Department of Earth and Environment, Boston University, Boston, MA, USA, from 2014 to 2016. He is an Assistant Professor with the School of Land Science and Techniques, China University of Geosciences, Beijing. He was involved in the generation and assessment of official MODIS/VIIRS global leaf area index (LAI) and fraction of photosynthetically active radiation absorbed by vegetation (fPAR) products. His research interests include the bidirectional reflectance distribution function (BRDF) modeling and LAI&fPAR retrieval.



**Wanjuan Song** received the B.S. degree in Geographic Information Science from the Beijing Normal University, Beijing, China, in 2013, and the Ph.D. degree in Cartography and Geography Information System from the Beijing Normal University, in 2019.

She was also a visiting scholar in the Department of Earth and Environment at Boston University, Boston, MA, USA, from 2016 to 2017. She is currently with the State Key Laboratory of Remote Sensing Science, Aerospace Information Research Institute, Chinese Academy of Science. Her research interests include the vegetation structure parameter estimation, vegetation remote sensing, and the application of DSCOVR EPIC data.



**Hanliang Li** was born in Shanxi province, China. He received the B.E. degree in the China University of Geosciences Beijing in 2020. He is currently pursuing the M.E. degree with the China University of Geosciences Beijing on remote sensing under the direction of Dr. Kai Yan



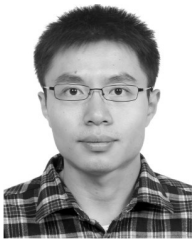
**Yiyi Tong** received the B.S. degree in physical geography and M.S. degree in remote sensing from Beijing Normal University, Beijing, China, in 2017 and 2020, respectively.

Her research interests include the estimation of radiation budget and validation of remote sensing models in rugged terrains.



**Dalei Hao** received the B.S. degree in surveying and mapping engineering from Wuhan University, Wuhan, China, in 2015. He is currently pursuing the Ph.D. degree with the Institute of Remote Sensing and Digital Earth, Chinese Academy of Sciences, Beijing, China.

He is currently a Visiting Scholar with the Joint Global Change Research Institute (JGCRI), Pacific Northwest National Laboratory (PNNL), College Park, MD, USA. His research interests include vegetation radiative transfer, radiation balance estimation, global carbon, cycle, and land surface modeling.



**Yelu Zeng** received the B.S. degree in remote sensing from Wuhan University, Wuhan, China, in 2011, and the Ph.D. degree from the Institute of Remote Sensing and Digital Earth, Chinese Academy of Sciences, Beijing, China, in 2016.

He is currently a Post-Doctoral Fellow with the Carnegie Institution for Science, Stanford, CA, USA. His research interests include 3-D radiative transfer modeling over vegetation canopies and solar-induced chlorophyll fluorescence (SIF).



**Xihan Mu** received the B.S. degree in computer science and technology from the College of Information Science and Technology, Beijing Normal University, Beijing, China, in 1999, and the Ph.D. degree in remote sensing from the School of Geography, Beijing Normal University, in 2009.

He was a Visiting Student with the Laboratoire des Sciences de l'Images, de l'Informatique et de la Télédétection, Louis Pasteur University, Strasbourg, France, in 2007, and a Visiting Scientist with the Commonwealth Scientific and Industrial Research Organization, Canberra, ACT, Australia, in 2016. He is currently with the State Key Laboratory of Remote Sensing Science, Faculty of Geographical Science, Institute of Remote Sensing Science and Engineering, Beijing Normal University. His research interests include multiangular remote sensing, particularly in the retrieval/measurement of vegetation structural parameters.



**Guangjian Yan** (Senior Member, IEEE) received the Ph.D. degree from the Institute of Remote Sensing Applications, Chinese Academy of Sciences, Beijing, China, in 1999.

He is a Professor with the State Key Laboratory of Remote Sensing Science, School of Geography, Beijing Normal University, Beijing. He has published more than 200 articles. His research interests include multiangular remote sensing, vegetation remote sensing, radiation budget, and scale correction of remote sensing.



**Ranga B. Myneni** received the Ph.D. degree in biology from the University of Antwerp, Antwerp, Belgium.

He is currently a Professor with Boston University, Boston, MA, USA. He is a Science Team Member of NASA MODIS and VIIRS projects. He has authored or co-authored over 250 scientific articles in peer-refereed journals. His research interests include remote sensing of vegetation and climate-vegetation interactions.



**Yuan Fang** received the B.Eng. and M.Sc. degrees in geomatics engineering from the China University of Geosciences, Beijing, China, in 2016 and 2018, respectively.

Her research interests include the hyperspectral imaging and environmental monitoring.



**Crystal Schaaf** received the B.S. and M.S. degrees in meteorology from the Massachusetts Institute of Technology, Cambridge, MA, USA, in 1982, the M.S. degree in archaeology from Harvard University, Cambridge, MA, USA, in 1988, and the Ph.D. degree in geography from Boston University, Boston, MA, USA, in 1994.

She served as an Atmospheric Research Officer with the United States Air Force, Cloud Physics Branch, USAF Geophysics Lab, Dayton, OH, USA, from 1982 to 1986. She was a Research Meteorologist with Satellite Branch, Geophysics Directorate, USAF Phillips Lab, Kirtland AFB, Albuquerque, NM, USA, from 1986 to 1996. She was a Research Assistant Professor with the Center for Remote Sensing, Department of Earth and Environment, Boston University, from 1996 to 2000, and a Research Associate Professor from 2000 to 2008. She was a Science Team Member and a Principal Investigator on Moderate Resolution Imaging Spectroradiometer on board NASA's Aqua and Terra Earth Observing System Platforms from 1999 to 2003. She has been a Science Team Member and a Principal Investigator for Visible/Infrared Imager/Radiometer Suite on board the Suomi National Polarorbiting Partnership and future NOAA/NASA Joint Polar Satellite Systems since 2004, a Science Team Member for Landsat Data Continuity Mission since 2012, and a Collaborator for Global Ecosystem Dynamics Investigation since 2014. She has been a Professor with the School for the Environment, University of Massachusetts Boston, Boston, MA, USA, since 2011. She has authored over 100 articles.